

Supplementary Information for

Machine Learning-Assisted Design of Flow Fields for Redox Flow Batteries

Shuaibin Wan^{a,1}, Haoran Jiang^{b,e,1}, Zixiao Guo^a, Changxiang He^a, Xiongwei Liang^a, Ned Djilali^{c,d,**}, Tianshou Zhao^{a,*}

^a Department of Mechanical and Aerospace Engineering, The Hong Kong University of Science and Technology, Clear Water Bay, Kowloon, Hong Kong SAR, China

^b Key Laboratory of Efficient Utilization of Low and Medium Grade Energy (MOE), Tianjin University, Tianjin, China

^c Department of Mechanical Engineering, University of Victoria, Victoria, BC, Canada

^d Institute for Integrated Energy Systems, University of Victoria, Victoria, BC, Canada

^e Institute for Advanced Study, The Hong Kong University of Science and Technology, Clear Water Bay, Kowloon, Hong Kong SAR, China

* Corresponding author

** Corresponding author

Email addresses: metzhao@ust.hk (T.S. Zhao), ndjilali@uvic.ca (N. Djilali)

¹ These authors contributed equally to this work.

Content

Supplementary Figures	4
Fig. S1	4
Fig. S2	4
Fig. S3	5
Fig. S4	5
Fig. S5	6
Fig. S6	6
Fig. S7	7
Fig. S8	7
Fig. S9	8
Fig. S10	8
Fig. S11	9
Fig. S12	10
Fig. S13	11
Fig. S14	11
Fig. S15	12
Fig. S16	12
Fig. S17	13
Fig. S18	14
Fig. S19	15
Fig. S20	15
Fig. S21	16
Fig. S22	16
Fig. S23	17
Fig. S24	17
Supplementary Tables.....	18
Table S1.....	18
Table S2.....	19
Table S3.....	20
Table S4.....	21

Table S5.....	22
Table S6.....	22
Supplementary Notes	23
Note S1	23
Note S2.....	30
Note S3.....	33
Supplementary References.....	34

Supplementary Figures

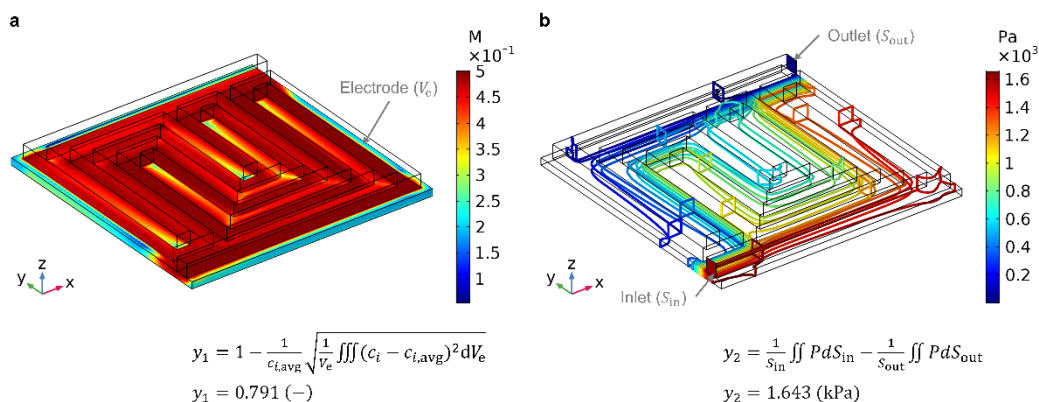


Fig. S1 Calculation method of the uniformity factor and the pressure drop. a) The uniformity factor (y_1) is calculated by the deviation of the V^{2+} concentration within the negative electrode. b) The pressure drop (y_2) is computed by the pressure difference between the inlet and outlet of the flow field. The calculation of y_1 and y_2 was realized by using the software COMSOL Multiphysics®.

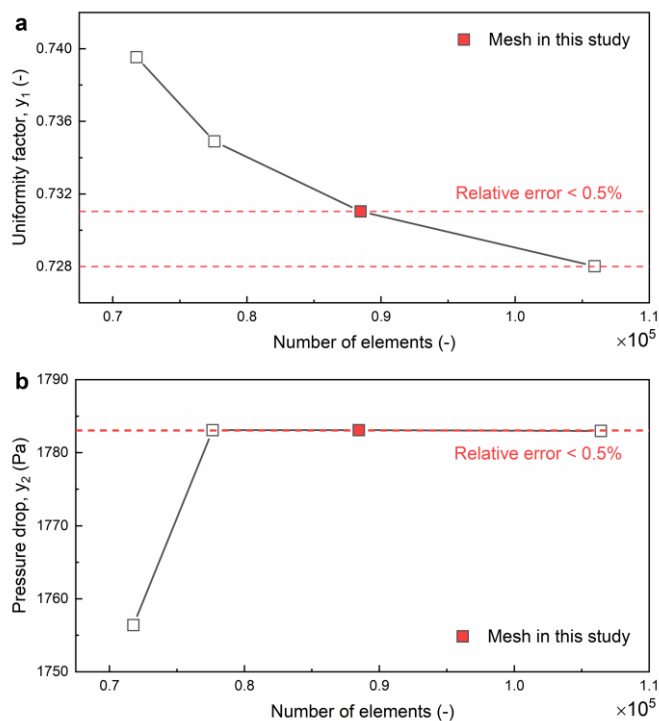


Fig. S2 Mesh sensitivity study performed by comparing the results of y_1 and y_2 with different mesh sizes, which are characterized by the number of elements. The simulation results are obtained at an area-specific flow rate of $3 \text{ mL} \cdot \text{min}^{-1} \cdot \text{cm}^{-2}$ and a discharge current density of $50 \text{ mA} \cdot \text{cm}^{-2}$, and the simulated geometry is the serpentine flow field.

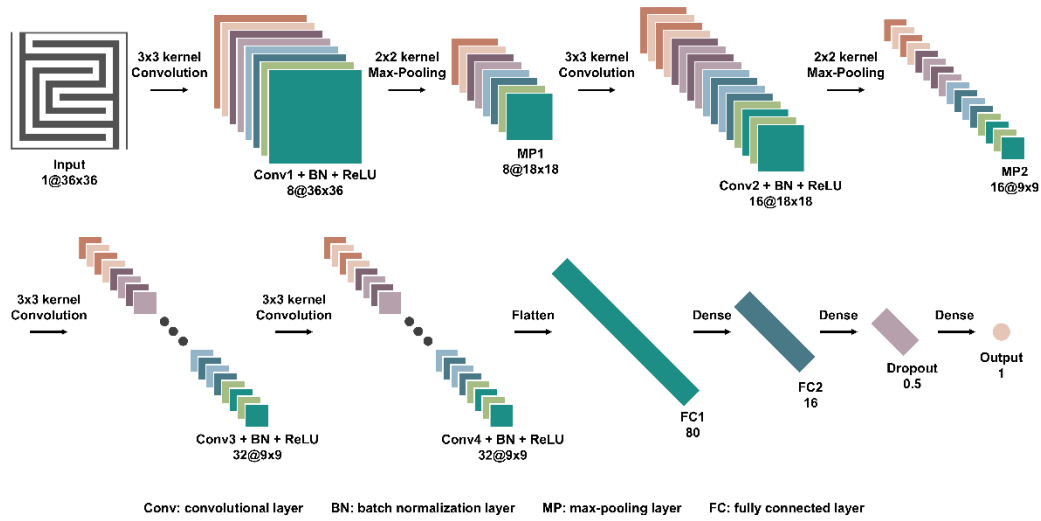


Fig. S3 Architecture of the convolutional neural network (CNN) used in this study. The network consists of 19 layers: one input layer, four convolutional layers, four batch normalization layers, four nonlinear layers, two max-pooling layers, two fully connected layers, one dropout layer, and one output layer. Note that the network architecture for predicting y_1 and y_2 is the same.

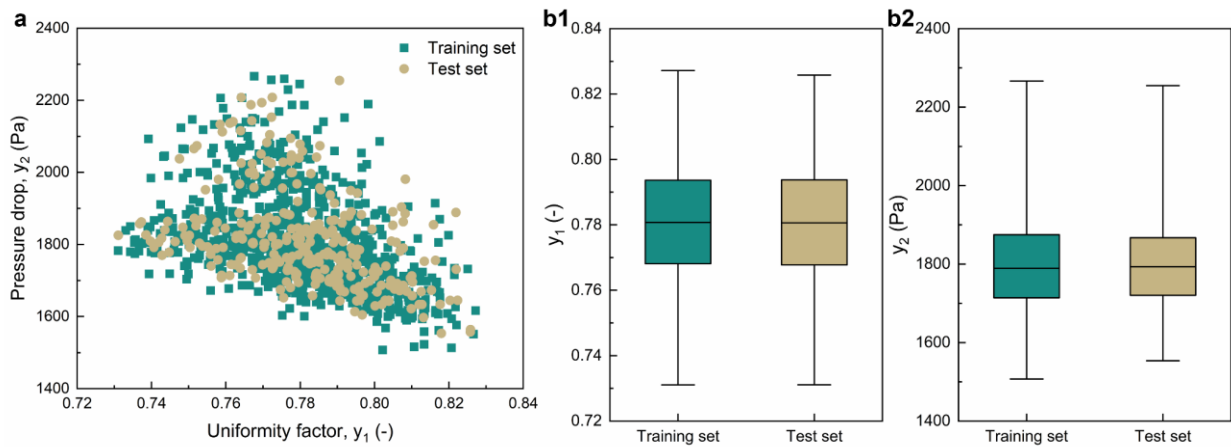


Fig. S4 a) Scatter plot of y_1 vs. y_2 showing the distribution of the training set (873 samples) and the test set (291 samples). b) Box-and-whisker plots comparing y_1 (b1) and y_2 (b2) of the two subsets. The bottom and top of the bar denote the first and third quartiles, and the band inside the box represents the median, and the whiskers outside the bar denote the maximum and minimum of the range.

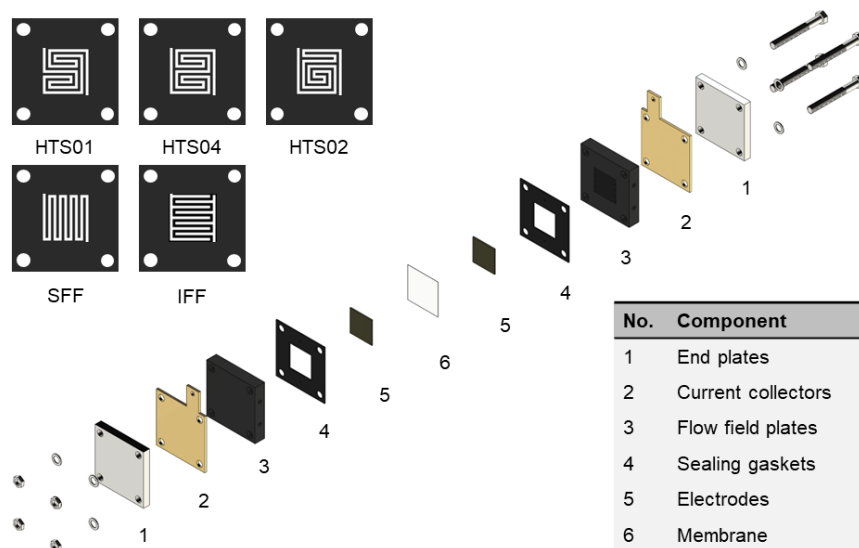


Fig. S5 Schematic of the VRFB tested in this study. The inserted table lists the key components of the battery system. A serpentine flow field (SFF) and an interdigitated flow field (IFF) were considered as benchmarks for evaluating the performance of the 3 new flow fields (HTS01, HTS04, and HTS02).

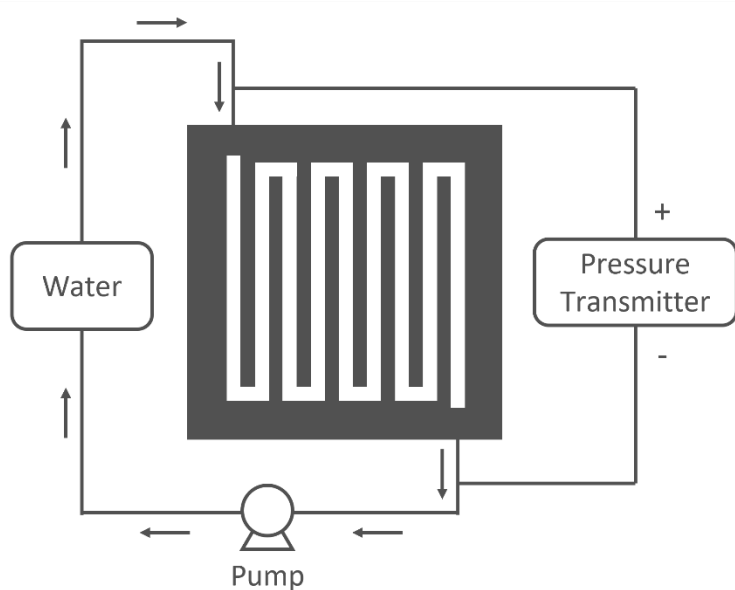


Fig. S6 Schematic of the pressure drop test. For convenience, water was used as the working medium. A pressure transmitter was used to measure the pressure difference between the inlet and outlet of the flow field plate.

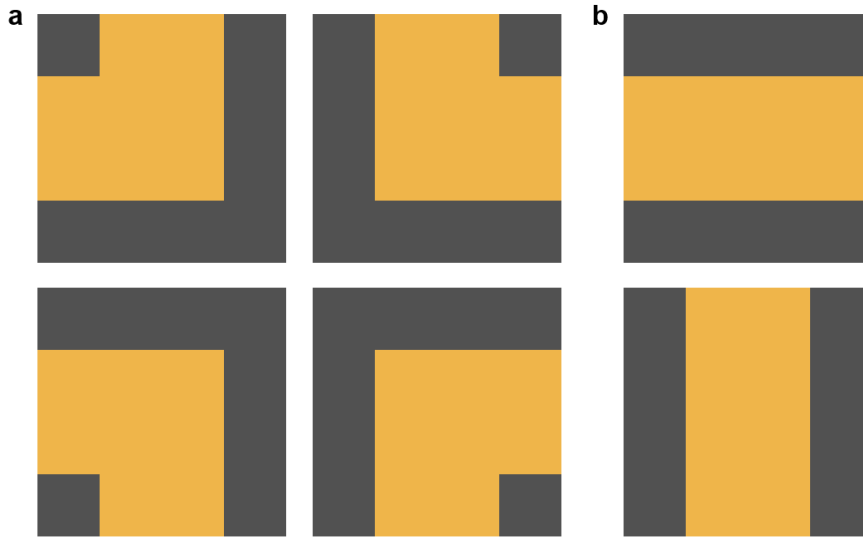


Fig. S7 Two types of cells in the flow field pattern: a) turn cells, and b) straight cells. There are four types of turn cells and two types of straight cells in total.

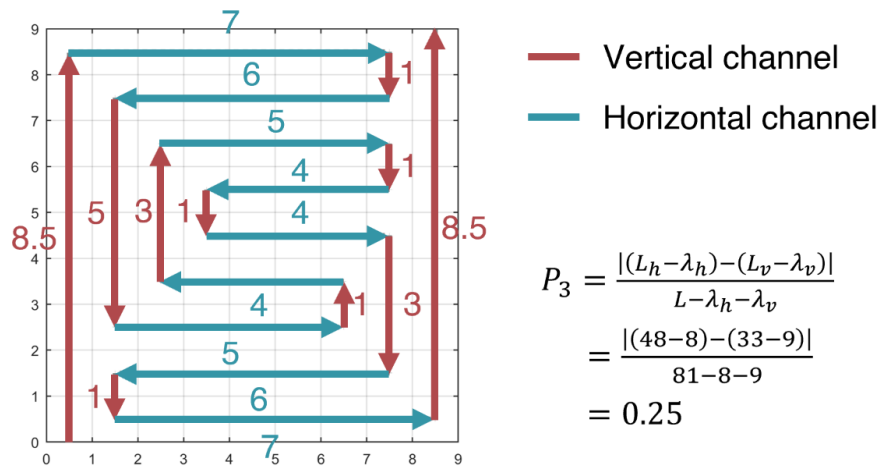


Fig. S8 Calculation method of the geometric property P_3 . Here the red and aqua solid lines denote the vertical and horizontal channels, respectively. As shown in the figure, the total length of horizontal channels is 48, and that of vertical channels is 33. Hence, the orientation bias (P_3) can be calculated as 0.25.

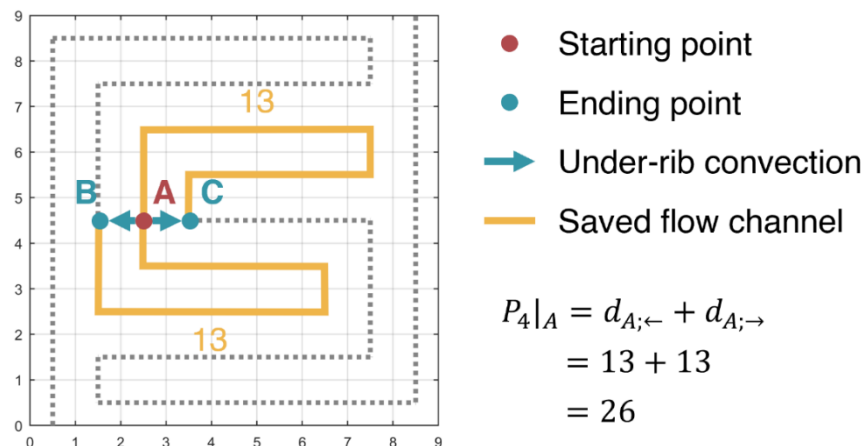


Fig. S9 Calculation method of the geometric property P_4 . Here only the vertex A (red point) is considered for demonstration purposes. The vertices B and C (aqua points) denote the neighboring channel region. If electrolytes at A move to B by under-rib convection (aqua arrow), it will save the channel length of 13 (gold solid line). Similarly, if electrolytes at A move to C by under-rib convection, it will save the channel length of 13. Hence, the saved channel length (P_4) for the vertex A is 26.

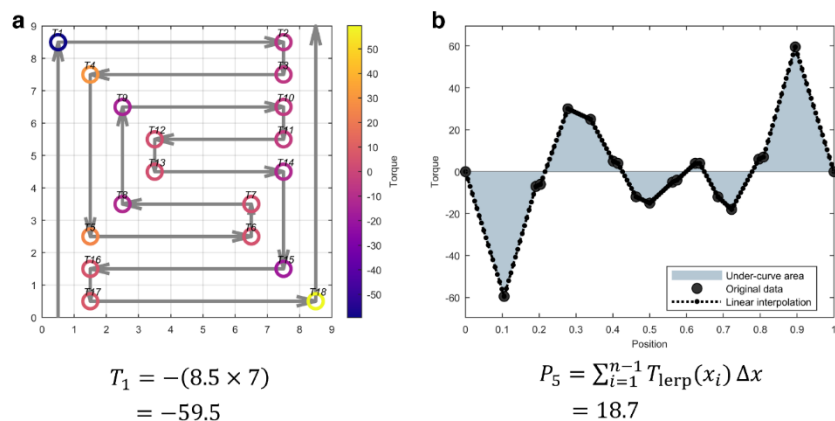


Fig. S10 Calculation method of the geometric property P_5 . The torque is defined as the cross product of the vectors of neighboring straight channels. For example, T_1 is calculated as -59.5 (a). After calculating the torque for all the turns, a torque distribution curve against the channel length can be obtained (black solid points in b). With linear interpolation (black dashed-dot line in b), the under-curve area (gray region in b) can be computed, which is exactly P_5 .

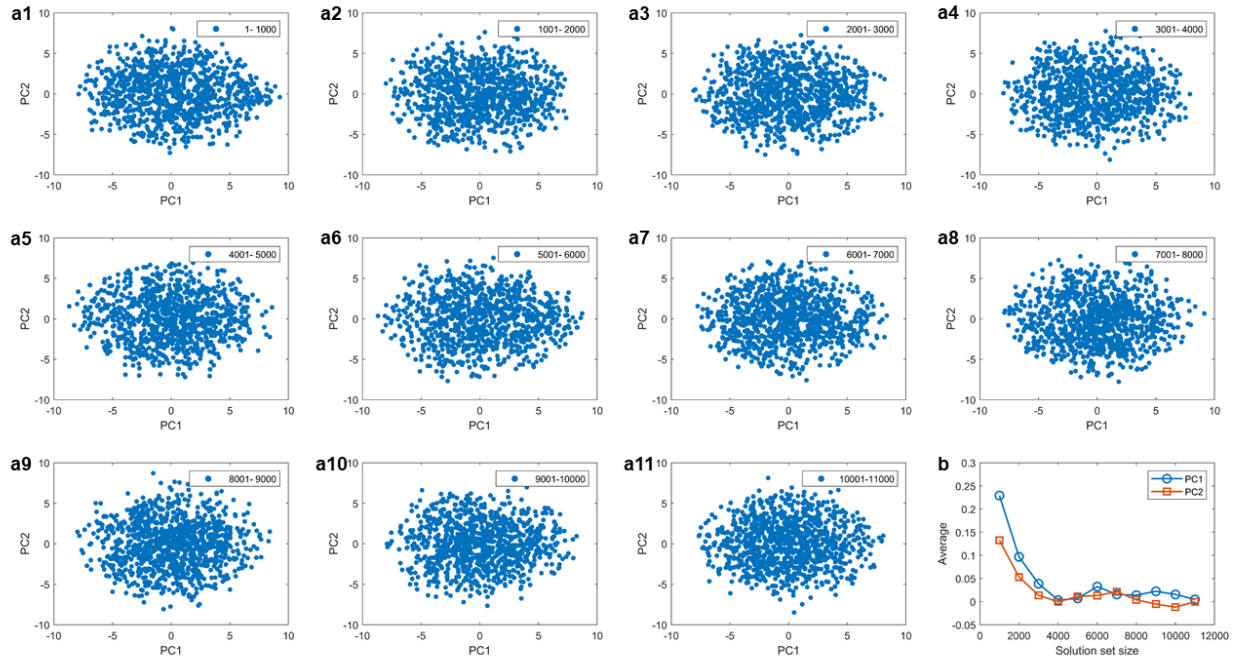


Fig. S11 a) Scatter plot of the first two principal components (denoted by PC1 and PC2) showing the distribution of the flow field images from No. 1 to No. 11,000. Among 1,236 components, PC1 and PC2 have the variance of 11.4% and 8.5%, respectively. Results show that the distribution of the flow field images generated in different stages is relatively stable, indicating that the path generation algorithm has no preferential direction for exploring the solution space. b) Average PC1 and average PC2 as a function of the solution set size. Results suggest that the set of the flow field images gradually reaches convergence when 4,000 solutions have been found. From the above results, we can infer that the subset collected in this study is sufficiently representative for the full solution set.

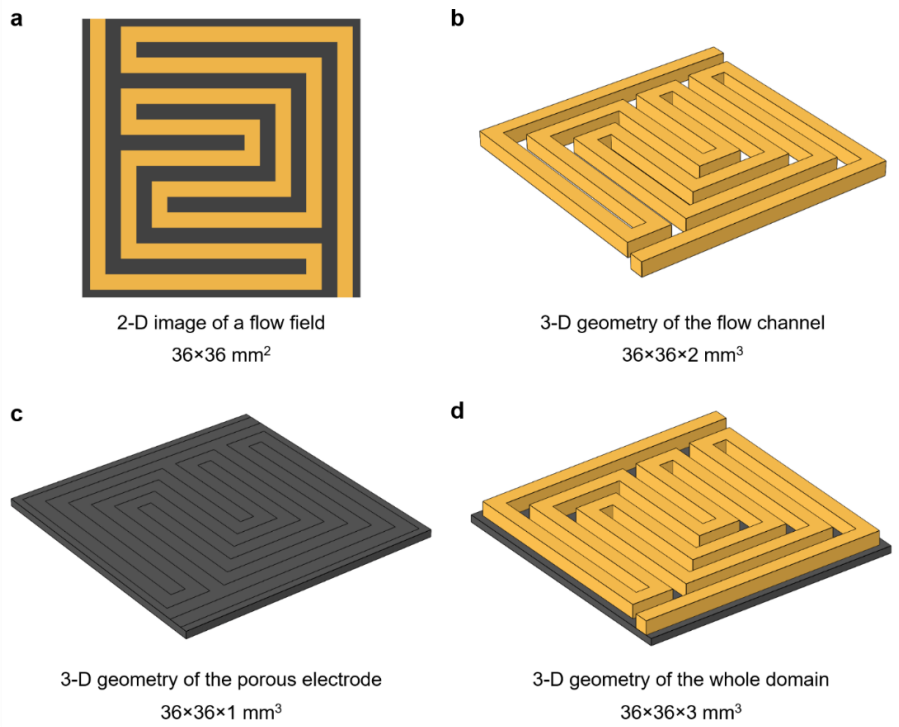


Fig. S12 Schematic illustrating how to convert a 2-D binary image into a 3-D geometry for the multi-physics simulation. a) 2-D binary image of a flow field with a dimension of $36 \times 36 \text{ mm}^2$. The channel and rib regions are colored in gold and black, respectively. b) 3-D geometry of the flow channel with a dimension of $36 \times 36 \times 2 \text{ mm}^3$. The geometry is obtained by extruding the channel region with a height of 2 mm (i.e., the channel depth is 2 mm). c) 3-D geometry of the porous electrode with a dimension of $36 \times 36 \times 1 \text{ mm}^3$ (i.e., the electrode thickness is 1 mm). The geometry is directly represented by a cuboid. d) 3-D geometry of the whole computational domain with a dimension of $36 \times 36 \times 3 \text{ mm}^3$. To perform simulation, the geometry shown in d) needs to be converted into face and vertex data (e.g., STL format); geometry conversion described above was realized by the software MATLAB.

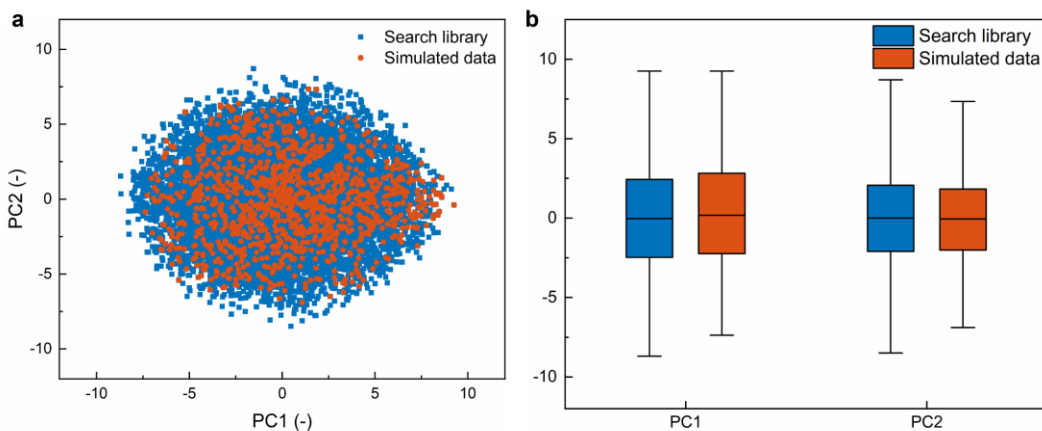


Fig. S13 a) Scatter plot of the first two principal component (denoted by PC1 and PC2) showing the distribution of the simulated dataset (1,164 samples) and the search library (11,564 samples). Among 1,236 components, PC1 and PC2 have the variance of 11.4% and 8.5%, respectively. b) Box-and-whisker plots comparing PC1 and PC2 of the simulated dataset and the search library. The bottom and top of the bar are the first and third quartiles, and the band inside the box represents the median, and the whiskers outside the bar denote the maximum and minimum of the range.

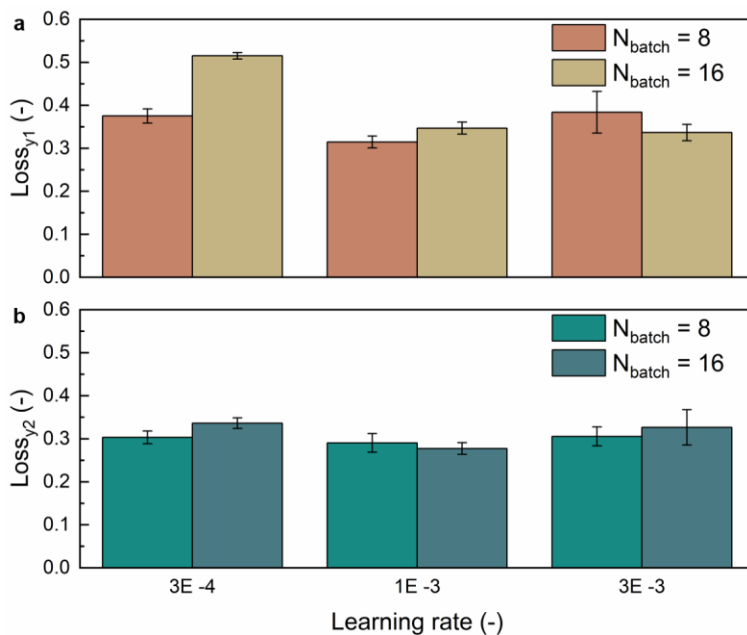


Fig. S14 Effect of hyper-parameters (here learning rate and mini-batch size) on the CNN performance for predicting y_1 (a) and y_2 (b). The bars show the mean value of five training results, and the whiskers denote the corresponding standard deviation. Before being fed to the CNN, the training data was normalized to improve the model stability, and thus the model loss was dimensionless.

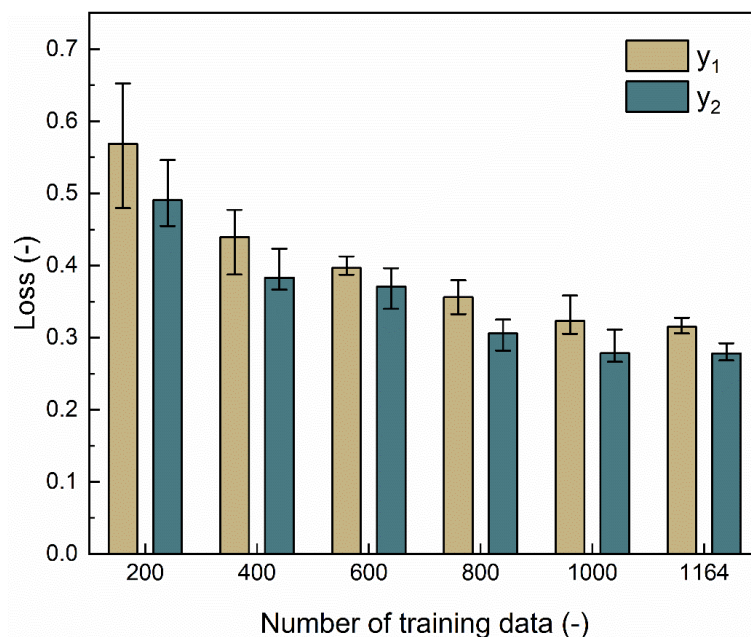


Fig. S15 Effect of the amount of training data on the CNN performance for predicting y_1 and y_2 . The bars show the mean value of five training results, and the whiskers denote the corresponding standard deviation. Here the CNN was trained on the data which were randomly selected from the original training dataset.

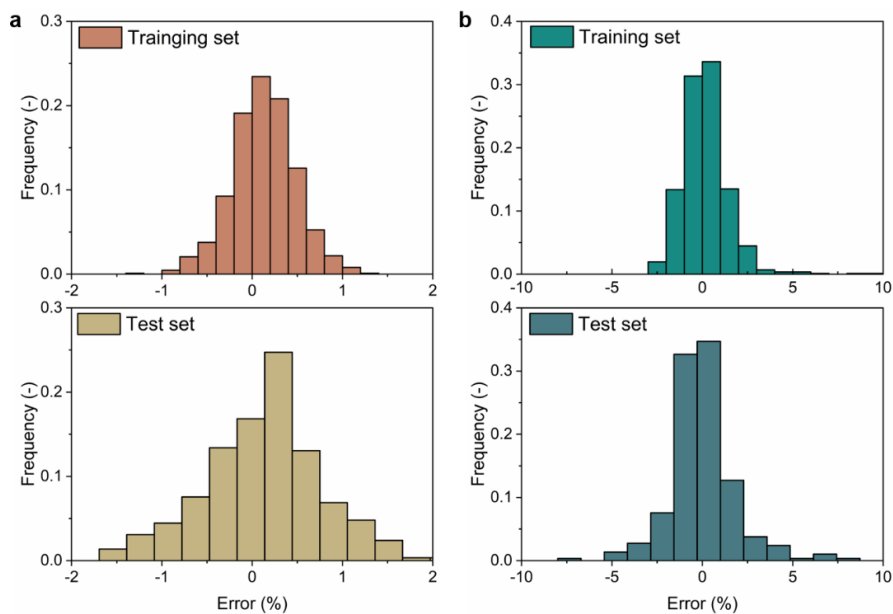


Fig. S16 Histogram plots of the prediction error for y_1 (a) and y_2 (b) on the training and test sets. Here the error was quantified using the mean absolute percentage error.

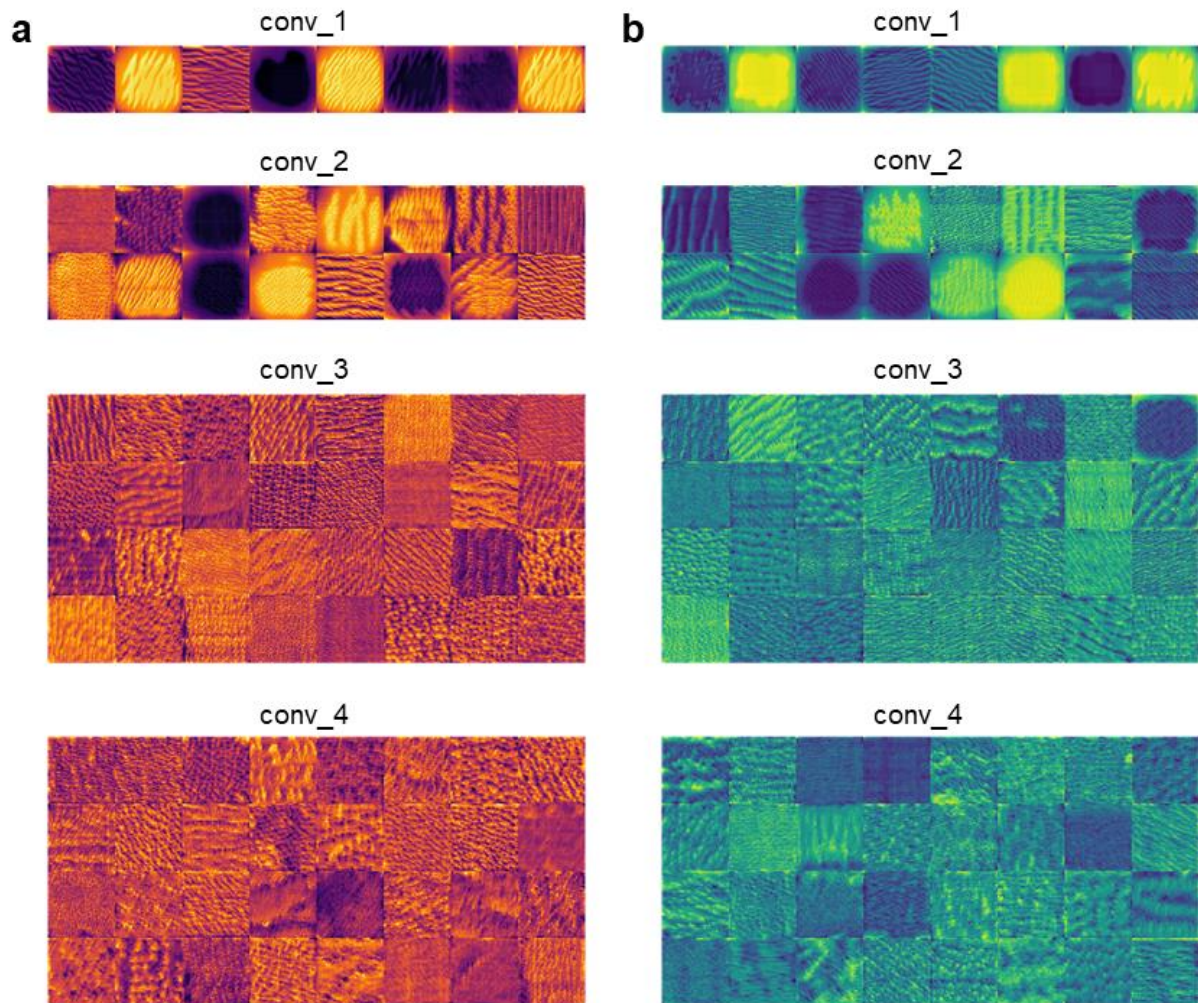


Fig. S17 Convolutional layers of the CNNs visualized by activation maximization. The CNN trained for predicting y_1 and y_2 is shown in (a) and (b), respectively. Here “conv” stands for convolutional layers, and the number behind the term denotes the order of the layer.

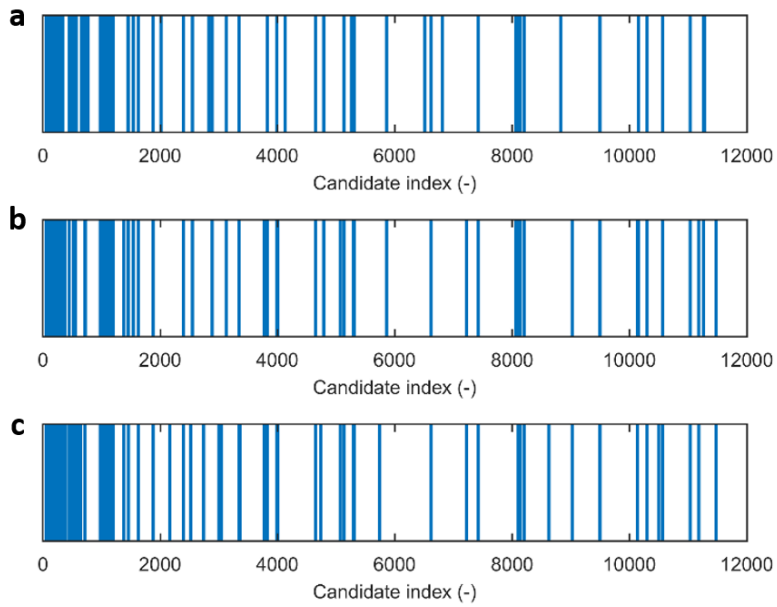


Fig. S18 Effect of the weighting factor (w) on the first-round screening result. Results show that the indices of the top 80 candidates remains almost unchanged with varying w from 0.3 (a), 0.5 (b), to 0.7 (c). This suggests that setting w as 0.5 in this study is adequate for screening optimal flow field designs.

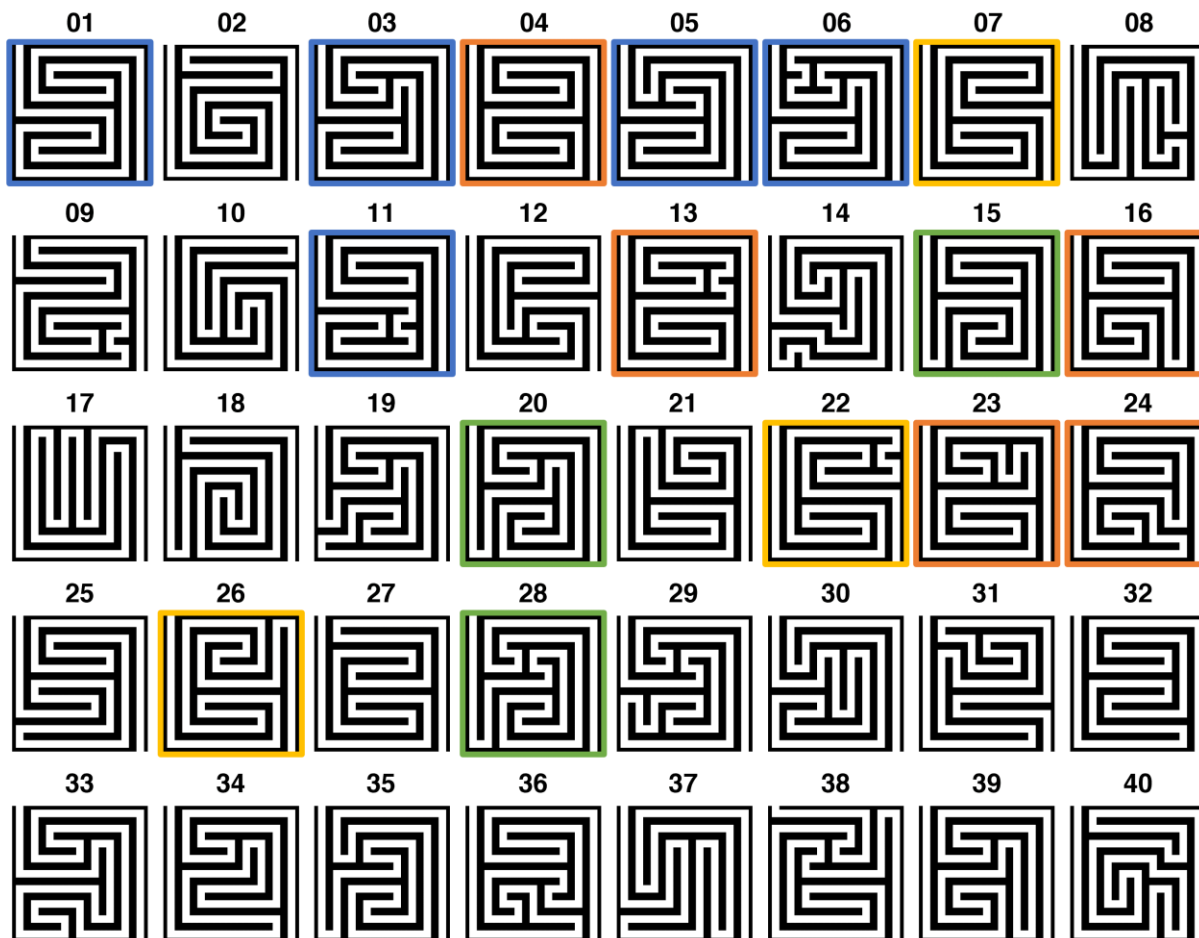


Fig. S19 Top 40 candidates selected from the first-round screening. An interesting finding is that there are some similar flow field designs, as highlighted in the same color. For example, HTS01 is quite similar to HTS03, HTS05, HTS06, HTS06, and HTS11. This phenomenon is reasonable because these similar flow field designs can be regarded as falling into the neighborhood of a local optimum in the solution space.

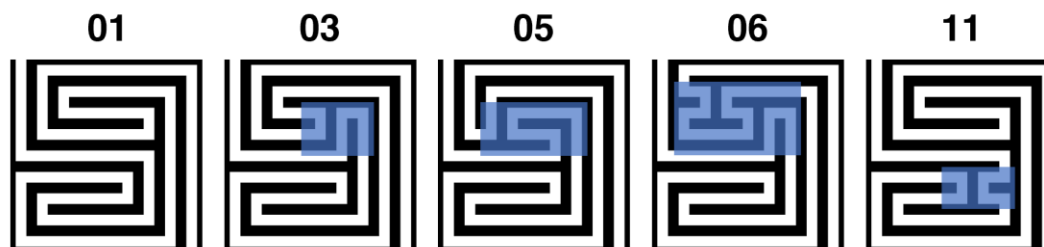


Fig. S20 Images of the HTS01, HTS03, HTS05, HTS06, and HTS11 flow fields. They have a similar pattern, and their differences are concentrated in a partial area (highlighted in blue).

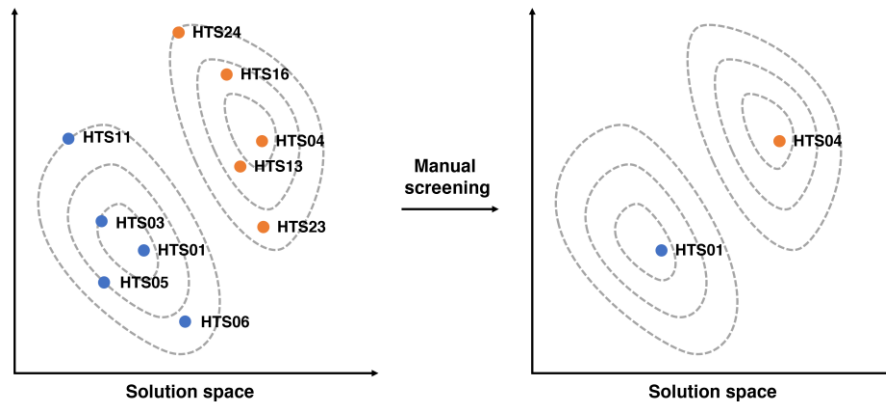


Fig. S21 Schematic demonstrating the role of manual screening in excluding flow field designs with similar patterns. Here flow field designs are represented as data points in the solution space. Similar flow field designs can be regarded as falling into the neighborhood of a local optimum, and their scores determine the distance to the local optimum. From similar candidates, experts only select the one that has earned the highest score in the first-round screening.

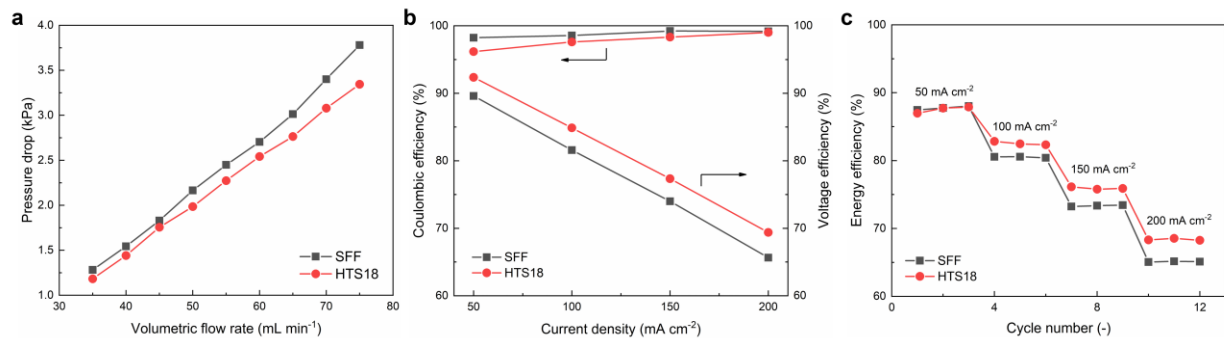


Fig. S22 Comparison of the HTS18 flow field with the SFF. a) Pressure drop of the battery with different flow fields at flow rates from 35 to 75 mL·min⁻¹. Here the results are given by the average of five measurements. b) Coulombic efficiency and voltage efficiency of the battery with different flow fields. c) Energy efficiency of the battery with different flow fields as a function of the charge-discharge cycle number.

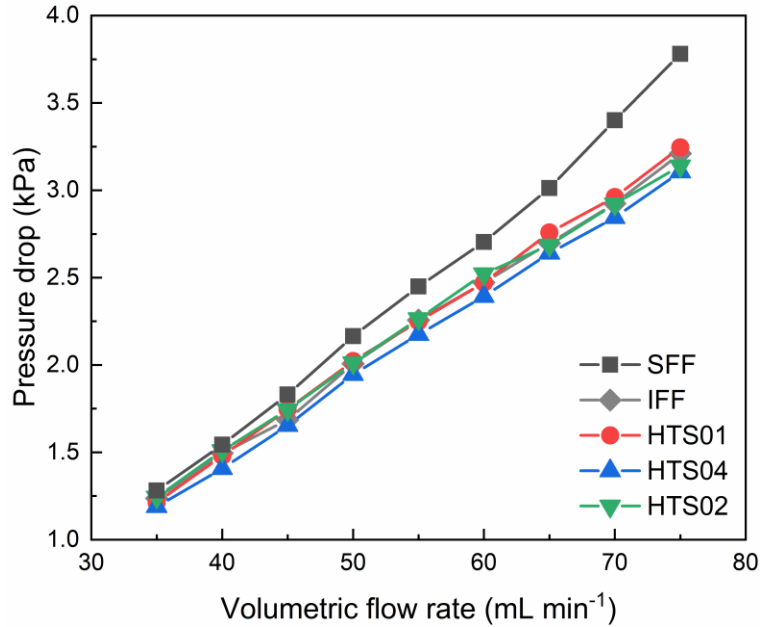


Fig. S23 Pressure drop of the battery with different flow fields at inlet flow rates ranging from 35 to 75 mL·min⁻¹. Here the results are given by the average of five measurements.

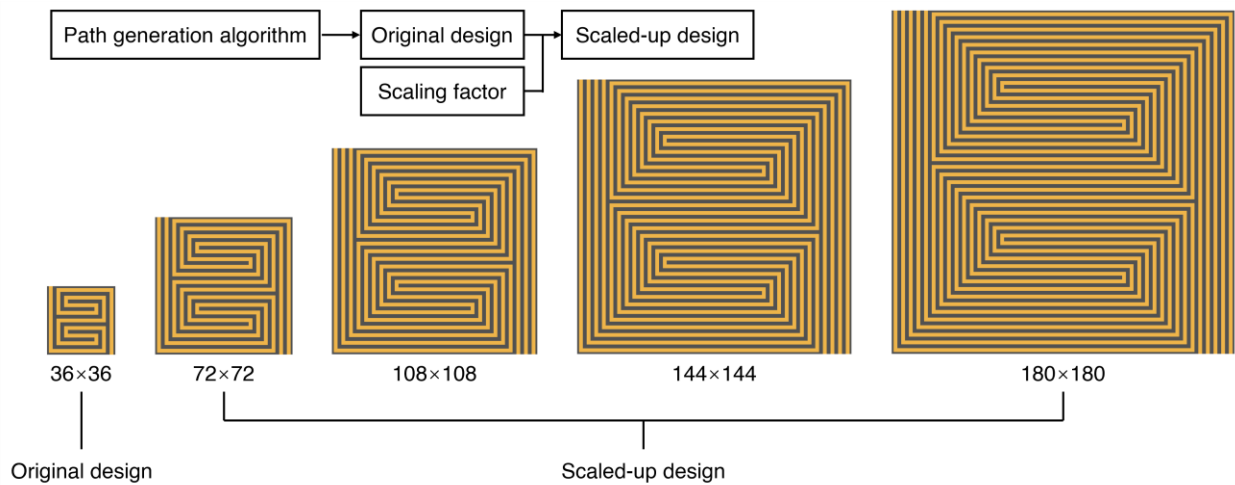


Fig. S24 Application of the path generation algorithm in scaled-up systems. Given a scaling factor, the algorithm can scale up the original design to a larger size. For demonstration purposes, the original design with a dimension of 36×36 mm² (one channel) can be easily scaled up to 72×72 mm² (two channels), 108×108 mm² (three channels), 144×144 mm² (four channels), 180×180 mm² (five channels) and more.

Supplementary Tables

Table S1 Model parameters of material properties and electrochemistry.

Symbol	Parameter	Value	Reference
ρ	Electrolyte density	$1.3 \times 10^3 \text{ kg} \cdot \text{m}^{-3}$	1
μ	Electrolyte viscosity	$4.928 \times 10^{-3} \text{ Pa} \cdot \text{s}$	2
ε	Compressed electrode porosity	0.79	Estimated
d_f	Mean fiber diameter	10 μm	3
k_{CK}	Carman-Kozeny constant	4.28	2
$D_{\text{V}^{2+}}$	Diffusion coefficient of V^{2+}	$2.4 \times 10^{-10} \text{ m}^2 \cdot \text{s}^{-1}$	4
$D_{\text{V}^{3+}}$	Diffusion coefficient of V^{3+}	$2.4 \times 10^{-10} \text{ m}^2 \cdot \text{s}^{-1}$	4
$D_{\text{VO}^{2+}}$	Diffusion coefficient of VO^{2+}	$3.9 \times 10^{-10} \text{ m}^2 \cdot \text{s}^{-1}$	4
$D_{\text{VO}_2^+}$	Diffusion coefficient of VO_2^+	$3.9 \times 10^{-10} \text{ m}^2 \cdot \text{s}^{-1}$	4
D_{H^+}	Diffusion coefficient of H^+	$9.3 \times 10^{-9} \text{ m}^2 \cdot \text{s}^{-1}$	2
a	Specific surface area	$2 \times 10^5 \text{ m}^{-1}$	5
$\alpha_{\text{a,neg}}$	Anodic charge transfer coefficient	0.5	6
$\alpha_{\text{c,neg}}$	Cathodic charge transfer coefficient	0.5	6
k_{neg}	Reaction rate constant (negative)	$1.7 \times 10^{-7} \text{ m} \cdot \text{s}^{-1}$	7
k_{pos}	Reaction rate constant (positive)	$6.8 \times 10^{-7} \text{ m} \cdot \text{s}^{-1}$	4
E_{neg}^0	Standard equilibrium potential	-0.255 V	8
E_{pos}^0	Standard equilibrium potential	+1.004 V	8
σ_s	Electronic conductivity of electrodes	$200 \text{ S} \cdot \text{m}^{-1}$	Manufacturer

Table S2 Model parameters related to boundary conditions.

Symbol	Parameter	Value
T	Operating temperature	298 K
SOC	State of charge	0.5
$c_{V^{2+}}^0$	Initial concentration of V^{2+}	500 mol·L ⁻³
$c_{V^{3+}}^0$	Initial concentration of V^{3+}	500 mol·L ⁻³
$c_{VO^{2+}}^0$	Initial concentration of VO^{2+}	500 mol·L ⁻³
$c_{VO_2^+}^0$	Initial concentration of VO_2^+	500 mol·L ⁻³
$c_{H^+}^0$	Initial concentration of H^+	1500 mol·L ⁻³
Q	Volumetric flow rate	35 ml·min ⁻¹
$i_{l,avg}$	Applied current density	50 mA·cm ⁻²

Table S3 Summary of the hyper-parameters used in the layers of the CNN.

Order	Layer name	Output shape	Other parameters
1	Input layer	36×36×1	-
2	Convolutional layer	36×36×8	kernel = [3, 3], stride = [1, 1], padding = 1
3	Batch normalization layer	36×36×8	-
4	ReLU layer	36×36×8	-
5	Max-pooling layer	18×18×8	kernel = [2, 2], stride = [2, 2]
6	Convolutional layer	18×18×16	kernel = [3, 3], stride = [1, 1], padding = 1
7	Batch normalization layer	18×18×16	-
8	ReLU layer	18×18×16	-
9	Max-pooling layer	9×9×16	kernel = [2, 2], stride = [2, 2]
10	Convolutional layer	9×9×32	kernel = [3, 3], stride = [1, 1], padding = 1
11	Batch normalization layer	9×9×32	-
12	ReLU layer	9×9×32	-
13	Convolutional layer	9×9×32	kernel = [3, 3], stride = [1, 1], padding = 1
14	Batch normalization layer	9×9×32	-
15	ReLU layer	9×9×32	-
16	Fully connected layer	1×1×80	-
17	Fully connected layer	1×1×16	-
18	Dropout layer	1×1×16	ratio = 0.5
19	Output layer	1×1×1	-

Note: ReLU stands for the rectified linear unit. The output shape is given in the form of $H \times W \times D$, where H and W denote the height and width of the feature map, and D denotes the number of feature maps.

Table S4 Summary of recent studies with manual screening involved in the discovery of novel materials. Note that some related works are not discussed because of space limitations.

Research object	Design variable	Reference
Organic light-emitting diode	Delayed fluorescence rate constant	9
Hybrid organic-inorganic perovskites for photovoltaics	Bandgap, thermal stability, toxicity	10
Polymer membrane for CO ₂ /CH ₄ separation	Permeability, selectivity, synthesis	11
Inorganic phosphor hosts for solid-state lighting	Debye temperature, bandgap	12
Solid-state electrolytes for lithium-ion batteries	Structural and chemical stability, electronic conductivity, cost, ionic conductivity	13
Superconductors	Critical temperature	14
NiTi-based shape memory alloys	Thermal hysteresis	15
BaTiO ₃ -based piezoelectrics	Electrostrain	16
Alkaline anion exchange membrane for fuel cells	Chemical stability	17
Solvents for producing porous polybenzimidazole membranes	Voltage efficiency, energy efficiency	18
Polymer	Glass transition temperature, bandgap	19
Polymer	Thermal conductivity	20

Table S5 Correlation matrix of p -values (p) between each two variables among the five geometric properties (P_1, P_2, P_3, P_4 , and P_5) and two output variables (y_1 and y_2).

	y_1	y_2	P_1	P_2	P_3	P_4	P_5
y_1	0	<0.001	fail	<0.001	<0.001	<0.001	<0.001
y_2	<0.001	0	<0.001	<0.001	<0.001	<0.001	<0.001
P_1	fail	<0.001	0	<0.001	<0.001	<0.001	<0.001
P_2	<0.001	<0.001	<0.001	0	<0.001	<0.001	<0.001
P_3	<0.001	<0.001	<0.001	<0.001	0	<0.001	<0.001
P_4	<0.001	<0.001	<0.001	<0.001	<0.001	0	<0.001
P_5	<0.001	<0.001	<0.001	<0.001	<0.001	<0.001	0

Note: In this study, the significance was checked at the 0.001 level, which means that the observed variables are statistically dependent if $p < 0.001$; otherwise, they are statistically independent (denoted by “fail” in the table).

Table S6 Comparison of the geometric properties of the 8 promising flow fields (denoted by “HTS”) with those of the serpentine flow field (SFF).

	P1 (-)	P2 (\bar{L})	P3 (-)	P4 (\bar{L})	P5 (\bar{L}^2)
HTS	18 ± 1	2.45 ± 0.16	0.23 ± 0.18	1490 ± 100	20.1 ± 1.8
SFF	16	3.66	1.00	640	4.45

Note: The results for the 8 promising candidates are given in the form of mean \pm standard deviation. Here \bar{L} denotes the unit length of flow channels.

Supplementary Notes

Note S1. 3-D multi-physics simulation

A 3-D multi-physics model was used to calculate the uniformity factor and pressure drop of 1,164 flow fields in the library. The model simulated physico-chemical phenomena occurring in the VRFB system, such as electrolyte flow, species and charge transport, and electrochemical reactions. For convenience, we first made the following assumptions^{1, 21, 22}: (I) all the physical processes were steady-state; (II) the electrolyte flow was incompressible; (III) all the material properties were isotropic and homogeneous; (IV) potential side reactions (e.g., hydrogen evolution) were not considered; (V) the dilute solution approximation was used; (VI) the second-step dissociation of sulfuric acid was neglected. In what follows, the governing equations and boundary conditions will be presented in detail.

The conservation of mass in the flow channel and electrode is given by the continuity equation:

$$\nabla \cdot \vec{u} = 0 \quad (\text{S1})$$

where \vec{u} is the velocity field of the electrolyte flow.

The conservation of momentum in the flow channel and porous electrode are described by the Navier-Stokes equation and the Brinkman equation, respectively:

$$\rho(\vec{u} \cdot \nabla)\vec{u} = -\nabla P + \mu\nabla^2\vec{u} \quad (\text{S2})$$

$$\frac{\rho}{\varepsilon^2}(\vec{u} \cdot \nabla)\vec{u} = -\nabla P + \frac{\mu}{\varepsilon}\nabla^2\vec{u} - \frac{\mu}{\kappa}\vec{u} \quad (\text{S3})$$

where ρ is the electrolyte density, P is the pressure field, μ is the electrolyte viscosity, ε is the electrode porosity, and κ is the hydraulic permeability of the porous electrode, which can be estimated by the Carman-Kozeny model²³:

$$\kappa = \frac{d_f^2 \varepsilon^3}{16k_{CK}(1-\varepsilon)^2} \quad (\text{S4})$$

where d_f is the mean fiber diameter of the porous electrode, and k_{CK} is the Carman-Kozeny constant that depends on the morphology of the porous media.

The transport of species in the electrolyte is driven by diffusion, migration, and convection, where the diffusion depends on the gradient of the species concentration, the migration depends on the electric field, and the convection depends on the electrolyte hydrodynamics. Based on the Nernst-Planck equation, the above transport phenomenon can be described by:

$$\nabla \cdot \left(-D_i^{\text{eff}} \nabla c_i - \frac{z_i c_i D_i^{\text{eff}}}{RT} F \nabla \phi_1 + c_i \vec{u} \right) = -S_i \quad (\text{S5})$$

where the subscript $i \in \{V^{2+}, V^{3+}, VO^{2+}, VO_2^+, H^+\}$, c_i is the molar concentration of the species i , z_i is the charge number, S_i is the source term, ϕ_1 is the electric potential in the electrolyte, R is the universal gas constant, T is the temperature, F is the Faraday constant, and D_i^{eff} is the effective diffusion coefficient of the species i . $D_i^{\text{eff}} = D_i$ for the flow channel, and $D_i^{\text{eff}} = \varepsilon^{1.5} D_i$ for the porous electrode, where D_i is the diffusion coefficient of the species i .

The source term of the species concentration is determined by the reaction rate, which is directly correlated with the local current density. At the negative side, the source terms of V^{2+} , V^{3+} , and H^+ are given by:

$$S_{V^{2+}} = \frac{a_{\text{loc,neg}}}{F} \quad (\text{S6})$$

$$S_{V^{3+}} = -\frac{ai_{loc,neg}}{F} \quad (S7)$$

$$S_{H^+} = 0 \quad (S8)$$

At the positive side, the source terms of VO^{2+} , VO_2^+ , and H^+ are given by:

$$S_{VO^{2+}} = \frac{ai_{loc,pos}}{F} \quad (S9)$$

$$S_{VO_2^+} = -\frac{ai_{loc,pos}}{F} \quad (S10)$$

$$S_{H^+} = -2\frac{ai_{loc,pos}}{F} \quad (S11)$$

where a is the specific surface area, and i_{loc} is the local current density in the electrode, which can be described by the Butler-Volmer equation:

$$i_{loc,neg} = i_{neg}^0 \left[\exp\left(\frac{\alpha_{a,neg}F\eta_{neg}}{RT}\right) - \exp\left(-\frac{\alpha_{c,neg}F\eta_{neg}}{RT}\right) \right] \quad (S12)$$

$$i_{loc,pos} = i_{pos}^0 \left[\exp\left(\frac{\alpha_{a,pos}F\eta_{pos}}{RT}\right) - \exp\left(-\frac{\alpha_{c,pos}F\eta_{pos}}{RT}\right) \right] \quad (S13)$$

where the subscripts neg and pos denote the negative and positive sides, respectively, α_a and α_c denote the anodic and cathodic charge transfer coefficients, respectively, η denote the overpotential, and i^0 denote the exchange current density, which is given by:

$$i_{neg}^0 = Fk_{neg}(c_{V^{2+}}^S)^{\alpha_{a,neg}}(c_{V^{3+}}^S)^{\alpha_{c,neg}} \quad (S14)$$

$$i_{pos}^0 = Fk_{pos}(c_{VO^{2+}}^S)^{\alpha_{a,pos}}(c_{VO_2^+}^S)^{\alpha_{c,pos}} \quad (S15)$$

where k is the reaction rate constant, and c_i^S represent the surface concentration of the species i at the electrode/electrolyte interface, which can be estimated by:

$$Fk_{m,neg}(c_{V^{2+}} - c_{V^{2+}}^S) = -Fk_{m,neg}(c_{V^{3+}} - c_{V^{3+}}^S) = i_{loc,neg} \quad (S16)$$

$$Fk_{m,\text{pos}}(c_{\text{VO}^{2+}} - c_{\text{VO}^{2+}}^s) = -Fk_{m,\text{pos}}(c_{\text{VO}_2^+} - c_{\text{VO}_2^+}^s) = i_{\text{loc, pos}} \quad (\text{S17})$$

where k_m is the local mass transport coefficient, which can be estimated by²⁴:

$$k_{m,\text{neg}} = k_{m,\text{pos}} = 1.6 \times 10^{-4} |\bar{u}|^{0.4} \quad (\text{S18})$$

In the Eq. S12 and S13, the overpotential (η) is expressed by:

$$\eta_{\text{neg}} = \phi_s - \phi_l - E'_{\text{neg}} \quad (\text{S19})$$

$$\eta_{\text{pos}} = \phi_s - \phi_l - E'_{\text{pos}} \quad (\text{S20})$$

where ϕ_s is the electric potential in the electrode, and E' is the equilibrium potential, which can be estimated by the Nernst equation:

$$E'_{\text{neg}} = E_{\text{neg}}^0 + \frac{RT}{F} \ln \left(\frac{c_{\text{V}^{3+}}}{c_{\text{V}^{2+}}} \right) \quad (\text{S21})$$

$$E'_{\text{pos}} = E_{\text{pos}}^0 + \frac{RT}{F} \ln \left[\frac{c_{\text{VO}_2^+} (c_{\text{H}^+})^2}{c_{\text{VO}^{2+}}} \right] \quad (\text{S22})$$

where E^0 is the standard equilibrium potential.

The charge transport in the electrode and electrolyte is respectively described by:

$$\nabla \cdot \vec{i}_s = -\sigma_s^{\text{eff}} \nabla^2 \phi_s = i_{\text{loc}} \quad (\text{S23})$$

$$\nabla \cdot \vec{i}_l = -\sigma_l^{\text{eff}} \nabla^2 \phi_l = -i_{\text{loc}} \quad (\text{S24})$$

where \vec{i}_s is the local current density in the electrode, \vec{i}_l is the local current density in the electrolyte, σ_s^{eff} is the effective electronic conductivity of the electrode, which is given by:

$$\sigma_s^{\text{eff}} = (1 - \varepsilon)^{1.5} \sigma_s \quad (\text{S25})$$

where σ_s is the electronic conductivity of the electrode. And σ_1^{eff} is the effective electronic conductivity of the electrolyte, which is given by⁶:

$$\sigma_{1,\text{neg}}^{\text{eff}} = 7.699 \times SOC + 35.716 \text{ (S m}^{-1}\text{)} \quad (\text{S26})$$

$$\sigma_{1,\text{pos}}^{\text{eff}} = 12.251 \times SOC + 43.763 \text{ (S m}^{-1}\text{)} \quad (\text{S27})$$

where SOC stands for the state of the charge, which can be defined as:

$$SOC = \frac{c_{V^{2+}}}{c_{V^{3+}} + c_{V^{2+}}} = \frac{c_{VO_2^+}}{c_{VO_2^+} + c_{VO_2^{\cdot+}}} \quad (\text{S28})$$

In this work, the uniformity factor of V^{2+} and the pressure drop are used to evaluate the performance of flow fields. The uniformity factor of V^{2+} is given by:

$$U_{V^{2+}} = 1 - \frac{1}{c_{V^{2+},\text{avg}}} \sqrt{\frac{1}{V_e} \iiint (c_{V^{2+}} - c_{V^{2+},\text{avg}})^2 dV_e} \quad (\text{S29})$$

where V_e denotes the volume of the electrode, and $c_{V^{2+},\text{avg}}$ represents the average concentration of V^{2+} . In addition, the pressure drop is determined by:

$$y_2 = \frac{1}{S_{\text{in}}} \iint P dS_{\text{in}} - \frac{1}{S_{\text{out}}} \iint P dS_{\text{out}} \quad (\text{S30})$$

where P denotes the pressure, and S_{in} and S_{out} denote the cross-sectional area of the inlet and the outlet, respectively (here $S_{\text{in}} = S_{\text{out}}$).

The boundary conditions related to the electrolyte flow are listed below. At the inlet, the velocity of the electrolyte flow is fixed, which are given by:

$$-\int \vec{u} \cdot \vec{n} dS_{\text{in}} = Q \quad (\text{S31})$$

where Q is the volumetric flow rate, and \vec{n} is the outward unit normal vector. At the outlet, the pressure is set as zero, as given by:

$$P = 0 \quad (\text{S32})$$

At the other walls, the no-slip boundary condition is used, which is given by:

$$\vec{u} = 0 \quad (\text{S33})$$

Then the boundary conditions related to the species transport are listed below. At the inlet, the concentration of electroactive species is fixed, as given by:

$$c_i = c_i^0 \quad (\text{S34})$$

where c_i^0 is the initial concentration of the species i . At the outlet, there is no diffusive flux, as given by:

$$\vec{n} \cdot D_i \nabla c_i = 0 \quad (\text{S35})$$

Finally, the boundary conditions related to the charge transport are listed below. At the rib surface at the negative side, the electric potential is assumed to be 0.

$$\phi_s = 0 \text{ (V)} \quad (\text{S36})$$

At the rib surface at the positive side, the electric potential is the equilibrium cell voltage.

$$\phi_s = E_{\text{pos}}^0 - E_{\text{neg}}^0 = 1.259 \text{ (V)} \quad (\text{S37})$$

At the bottom surface of the electrode, an average current density is applied.

$$\int \vec{i}_l \cdot \vec{n} dS = i_{l,\text{avg}} \int dS_e \quad (\text{S38})$$

where S_e denotes the area of the electrode bottom, and $i_{l,avg}$ is the applied current density, which is a negative value for the negative side and is a positive value for the positive side. On the other external walls, the insulation boundary condition is applied.

$$-\vec{n} \cdot \vec{i}_l = 0 \quad (S39)$$

$$-\vec{n} \cdot \vec{i}_s = 0 \quad (S40)$$

The model parameters of material properties and electrochemistry are listed in Table S1. The parameters related to boundary conditions are listed in Table S2. The simulation was performed using the software COMSOL Multiphysics[®] with the built-in interfaces of Free and Porous Media Flow, Secondary Current Distribution, and Transport of Dilute Species. The swept mesh with around 100,000 elements was used, and the relative tolerance of the solver was set as 1×10^{-3} based on the balance between the accuracy and the computational cost.

Note S2. Convolutional neural networks

Convolutional neural networks (CNNs)²⁵⁻²⁷ were used to capture the mapping of the input variables to the output variables. Note that the CNN belongs to the category of deep learning, which is a subset of machine learning, and thus both the terms are used in the literature of CNN applications. Here, the input variable is a 36×36 binary image that represents a flow field, and the output variables are the uniformity factor and pressure drop of the corresponding flow field. In this work, the CNN was constructed using 19 layers: one input layer, four convolutional layers, four batch normalization layers, four ReLU layers, two max-pooling layers, two fully connected layers, one dropout layer, and one output layer, as shown in Fig. S3. In what follows, we will describe the function of the layers mentioned above.

(1) Convolutional layer. A convolutional layer convolves filters with the input image to extract feature maps. Specifically, suppose that the input in the l -th layer (x^l) is a 3-D tensor with a size of $H^l \times W^l \times D^l$, and the convolution filter is then a 3-D tensor with a size of $F \times F \times D^l$. The convolutional layer computes the dot product of the filter with the corresponding elements of the input image across all the D^l channels. Meanwhile, the filter slides over the entire input image to compute the convolution. Very often, multiple filters are used in a convolutional layer to obtain different feature maps. Assuming that the number of filters is K , the filter (w) is then a 4-D tensor with a size of $F \times F \times D^l \times K$. It is trivial to know that the size of the output (x^{l+1}) of the convolutional layer is:

$$(H^l - F + 1) \times (W^l - F + 1) \times K \quad (\text{S41})$$

Hence, the spatial extent of the output is smaller than that of the input as long as the filter has a spatial extent larger than 1×1 . It is, however, useful to make the input and output have the same

height and weight, and thus a zero-padding trick was widely used. That is, elements of 0 are added outside of the four edges of the input. Generally, the size of the zero padding can be determined by:

$$\left(\frac{F-1}{2}\right) \times \left(\frac{F-1}{2}\right) \quad (\text{S42})$$

Furthermore, stride is another important hyper-parameter in a convolutional layer. To convolve filters with each spatial location of the input, the stride was set as 1 in this study. Moreover, a bias term (b) is usually needed in a convolutional layer. Taken together, the convolution operation can be described by:

$$x_{i^{l+1},j^{l+1},k}^{l+1} = \sum_{i=1}^F \sum_{j=1}^F \sum_{d=1}^{D^l} w_{i,j,d,k}^l \times x_{i^{l+1}+i,j^{l+1}+j,d^l}^l + b_k \quad (\text{S43})$$

where $0 \leq k \leq K$.

(2) ReLU layer. The rectified linear unit (ReLU) layer is the most widely used non-linearity in CNNs, mainly because the ReLU is very easy to compute. Note that there is no learnable parameter in a ReLU layer, and the ReLU layer does not change the size of the input. Suppose that the input (x^l) is a 3-D tensor with a size of $H^l \times W^l \times D^l$, and then the output (x^{l+1}) can be given by:

$$x_{i,j,d}^{l+1} = \max\{0, x_{i,j,d}^l\} \quad (\text{S44})$$

where $1 \leq i \leq H^l = H^{l+1}$, $1 \leq j \leq W^l = W^{l+1}$, and $1 \leq d \leq D^l = D^{l+1}$.

(3) Max-pooling layer. A max-pooling layer is aimed at selecting the local maximum on the feature maps and meanwhile reduce the number of learnable parameters in the subsequent layers. As does in convolutional layers, a max-pooling layer uses a filter to slide over the entire input image to complete the operation, but the difference is that the movement of the slide in the max-pooling layer is non-overlapping. Suppose that the input (x^l) is a 3-D tensor with a size of $H^l \times W^l \times D^l$,

and the input is then divided into $H^{l+1} \times W^{l+1}$ non-overlapping subregions by a filter with a spatial extent of $F \times F$. That is, the size of the output (x^{l+1}) is:

$$\frac{H^l}{F} \times \frac{W^l}{F} \times D^l \quad (\text{S45})$$

In a max-pooling layer, the maximum value for each sub-region is selected, as given by:

$$x_{i^{l+1}, j^{l+1}, d^l}^{l+1} = \max_{1 \leq i \leq F, 1 \leq j \leq F} x_{i^{l \times F + i}, j^{l \times F + j}, d^l}^l \quad (\text{S46})$$

where $1 \leq d^l \leq D^l$. In this work, the filter size was set as 2×2 , and then the stride was 2.

(4) Fully connected layer. Fully connected layers are useful to integrate the feature maps extracted by the previous convolution, ReLU, and pooling operations. Essentially, a fully connected layer is exactly a convolutional layer that involves all the elements of the input in the convolution. Suppose that the input is a 3-D tensor with a size of $H^l \times W^l \times D^l$, then the tensor is flattened to a 1-D tensor with the length of $H^l W^l D^l$. Given that the number of nodes is K , the filter has a size of $H^l W^l D^l \times K$, and the output of the fully connected layer is in \mathbb{R}^K . In this work, two connected fully layers with 80 and 16 nodes were used.

(5) Dropout layer. A dropout layer is a technique to improve the generalization of CNNs. In this layer, a dropout probability is required to specify the proportion of nodes connected to the network. In this work, the dropout probability was set as 0.5.

Note S3. Statistical analysis tools

Given that the data is non-Gaussian, Spearman's rank correlation coefficient was used to estimate the association strength between the two variables studied. Specifically, the Spearman's rank correlation coefficient assesses the degree to which a pair of variables are monotonically related²⁸. Its value varies from -1 to +1, where the negative sign indicates a negative correlation and the positive sign indicates a positive correlation, and the magnitude represents how strong the relationship is²⁹. In addition, the p -value was used to quantify the statistical dependence between the two variables. In this study, we checked for significance at the 0.001 level, which means that the two variables observed will be correlated significantly if the p -value is less than 0.001; otherwise, they are probably independent to each other. In this work, Spearman's rank correlation coefficients and p -values were calculated using MATLAB.

Supplementary References

1. C. Yin, Y. Gao, S. Guo and H. Tang. *Energy*, 2014, **74**, 886-895
2. D. You, H. Zhang and J. Chen. *Electrochim. Acta*, 2009, **54**, 6827-6836
3. H. R. Jiang, W. Shyy, M. C. Wu, R. H. Zhang and T. S. Zhao. *Appl. Energy*, 2019, **233**, 105-113
4. T. Yamamura, N. Watanabe, T. Yano and Y. Shiokawa. *J. Electrochem. Soc.*, 2005, **152**, A830
5. H. R. Jiang, B. W. Zhang, J. Sun, X. Z. Fan, W. Shyy and T. S. Zhao. *J. Power Sources*, 2019, **440**, 227159
6. B. W. Zhang, Y. Lei, B. F. Bai and T. S. Zhao. *Int. J. Heat Mass Transfer*, 2019, **135**, 460-469
7. E. Sum and M. Skyllas-Kazacos. *J. Power Sources*, 1985, **15**, 179-190
8. A. A. Shah, H. Al-Fetlawi and F. C. Walsh. *Electrochim. Acta*, 2010, **55**, 1125-1139
9. R. Gómez-Bombarelli, J. Aguilera-Iparraguirre, T. D. Hirzel, D. Duvenaud, D. Maclaurin, M. A. Blood-Forsythe, H. S. Chae, M. Einzinger, D. Ha and T. Wu. *Nature materials*, 2016, **15**, 1120
10. S. Lu, Q. Zhou, Y. Ouyang, Y. Guo, Q. Li and J. Wang. *Nature communications*, 2018, **9**, 3405
11. J. W. Barnett, C. R. Bilchak, Y. Wang, B. C. Benicewicz, L. A. Murdock, T. Bereau and S. K. Kumar. *Science advances*, 2020, **6**, eaaz4301
12. Y. Zhuo, A. Mansouri Tehrani, A. O. Oliynyk, A. C. Duke and J. Brgoch. *Nature communications*, 2018, **9**, 1-10
13. A. D. Sendek, Q. Yang, E. D. Cubuk, K. N. Duerloo, Y. Cui and E. J. Reed. *Energy & Environmental Science*, 2017, **10**, 306-320
14. V. Stanev, C. Oses, A. G. Kusne, E. Rodriguez, J. Paglione, S. Curtarolo and I. Takeuchi. *npj Computational Materials*, 2018, **4**, 29
15. D. Xue, P. V. Balachandran, J. Hogden, J. Theiler, D. Xue and T. Lookman. *Nature communications*, 2016, **7**, 1-9
16. R. Yuan, Z. Liu, P. V. Balachandran, D. Xue, Y. Zhou, X. Ding, J. Sun, D. Xue and T. Lookman. *Adv Mater*, 2018, **30**, 1702884

17. X. Zou, J. Pan, Z. Sun, B. Wang, Z. Jin, G. Xu and F. Yan. *Energy & Environmental Science*, 2021, **14**, 3965-3975
18. T. Li, W. Lu, Z. Yuan, H. Zhang and X. Li. *Journal of Materials Chemistry A*, 2021, **9**, 14545-14552
19. C. Kim, R. Batra, L. Chen, H. Tran and R. Ramprasad. *Computational Materials Science*, 2021, **186**, 110067
20. S. Wu, Y. Kondo, M. Kakimoto, B. Yang, H. Yamada, I. Kuwajima, G. Lambard, K. Hongo, Y. Xu and J. Shiomi. *npj Computational Materials*, 2019, **5**, 5
21. G. Qiu, C. R. Dennison, K. W. Knehr, E. C. Kumbur and Y. Sun. *J. Power Sources*, 2012, **219**, 223-234
22. Z. Cheng, K. M. Tenny, A. Pizzolato, A. Forner-Cuenca, V. Verda, Y. Chiang, F. R. Brushett and R. Behrou. *Appl. Energy*, 2020, **279**, 115530
23. J. T. Gostick, M. W. Fowler, M. D. Pritzker, M. A. Ioannidis and L. M. Behra. *J. Power Sources*, 2006, **162**, 228-238
24. D. Schmal, J. Van Erkel and P. J. Van Duin. *J. Appl. Electrochem.*, 1986, **16**, 422-430
25. J. Wu. *National Key Lab for Novel Software Technology. Nanjing University. China*, 2017, **5**, 23
26. S. Albawi, T. A. Mohammed & S. Al-Zawi. 2017 International Conference on Engineering and Technology (ICET), 2017
27. K. O'Shea and R. Nash. *arXiv preprint arXiv:1511.08458*, 2015,
28. J. L. Myers, A. Well and R. F. Lorch. in *Research design and statistical analysis* , Routledge, 2010
29. D. J. Benjamin, J. O. Berger, M. Johannesson, B. A. Nosek, E. Wagenmakers, R. Berk, K. A. Bollen, B. Brembs, L. Brown and C. Camerer. *Nature Human Behaviour*, 2018, **2**, 6-10